Calibration of a Triaxial, Consumer-grade Magnetometer via an Extended Two-step Methodology

Rogério P. Menezes Filho[1] Felipe O. Silva[2]
Leonardo A. Vieira[3] Lucas P. S. Paiva[4] Gustavo S. Carvalho[5]

Department of Automatics, Federal University of Lavras, MG (emails: rogeriofilho03@gmail.com[1], felipe.oliveira@ufla.br[2], laviera1992@hotmail.com[3], paiva.lucasps@gmail.com[4], guhcarv93@gmail.com[5]).

Abstract: Humans have always had the necessity of estimating their location in space for various reasons, e.g. hunting, traveling, sailing, battling, etc. Today, many other areas also demand that information, such as aviation, agriculture, multiple smartphone applications, law enforcement, and even film industry, to mention but a few. Estimating position and orientation is known as navigation, and the means to achieve it are called navigation systems. Each approach has its pros and cons, but sometimes it is possible to combine them into an improved architecture. For instance, inertial sensors (i.e. accelerometers and gyroscopes) can be integrated with magnetometers, producing an Attitude and Heading Reference System (AHRS); this process is referred to as sensor fusion. However, before sensors can be used to produce the navigation solution, calibration is often necessary, especially for low-cost devices. In this study, we perform the calibration of a triaxial consumer-grade magnetometer via an extended two-step methodology, correct small mistakes present in the original paper, and evaluate the technique in a restricted motion scenario. This technique can be implemented in-field, simply by rotating the sensors to multiple orientations; the only external information necessary is the local Earth's magnetic field density, easily estimated through reliable models. The error parameters, i.e. biases, scale factors, and misalignments, are indirectly estimated via a least squares algorithm. The calibration is first performed through software simulation, followed by hardware implementation to validate the results.

Keywords: Navigation Systems, Calibration, Magnetometer, AHRS, Low-cost sensors.

1. INTRODUCTION

Magnetometers are versatile sensors that can operate in a variety of applications, with different working principles. For instance, they are used as speedometers for some kinds of motors, as digital compasses for navigation, or for other applications that require measurements of magnetic field density. For the purpose of this work, we are interested in magnetometers used as part of navigation systems, which fall into four categories: fluxgates, Hall-effect, magnetoinductive, or magnetoresistive sensors (Groves, 2013).

Humans have relied on Earth's magnetic field for navigation since ancient times; Chinese people developed one of the first compasses, with a floating plate containing a magnetic lodestone (Renaudin et al., 2010). Since then, technology has greatly evolved; and today we can buy a consumer-grade digital magnetometer, such as the Honeywell HMC5883L, for only a few dollars. These sensors are especially useful for integrated navigation, which combines multiple technologies in order to produce a more precise and reliable navigation solution with a low budget (Gebre-Egziabher et al., 1996; Sheng and Zhang, 2015). AHRSs (Attitude and Heading Reference Systems) are one of the many approaches for integrated navigation, combining magnetic and inertial sensors.

However, and as particularly discussed in Section 2, magnetometers are affected by a number of error components that corrupt its measurements, especially in low-cost devices. If not handled, these errors can deeply compromise or even preclude navigation. The usual approach to manage this problem is calibration, i.e., estimating error parameters and correcting measurements. This topic has been broadly addressed and many techniques have been developed throughout the years. On the other hand, such procedures may not be so trivial, and deserve a closer look.

One of the most popular methods for magnetometer calibration is known as compass swinging (Bowditch, 1995). It consists of rotating magnetometers to multiple directions, while an external, reliable source of orientation is used to track the movements; finally, a non-linear parameter esti-

mation is performed to map the relation between measured and ground-truth orientations. Nevertheless, depending on an external source of orientation is an undesirable shortcoming, as stated by Alonso and Shuster (2002a), who presented a technique based on the work of Gambhir (1975) to overcome this issue. The same authors extended their work for a more extensive calibration, estimating more error parameters (Alonso and Shuster, 2002b); Crassidis et al. (2005) also claimed relevant improvements to this work.

Afterwards, Gebre-Egziabher et al. (2006) also addressed some issues involving compass swinging, namely: (a) the need for an external attitude source, (b) the requirement for the sensor to be horizontally leveled, and (c) the location dependency. Their so-called two-step technique is based on the idea that if a perfect, uncorrupted triaxial magnetometer (also applies for 2D) is rotated around itself, the magnitude of the sensors readings would lie on a sphere manifold, with radius equal to the local Earth's magnetic field density. However, as measurements are corrupted, the sphere becomes a rotated, shifted ellipsoid. Therefore, the error parameters can be derived from the ellipsoid estimation, performed via a straightforward least squares algorithm.

Although Gebre-Egziabher et al. (2006) were successful with their method, they did not consider some relevant error parameters. In order to include these parameters, Foster and Elkaim (2008) presented one of the most cited calibration algorithms, an extended version of the two-step technique that estimates the most important systematic error components of a magnetometer. Other methods were presents in sequence, such as (Vasconcelos et al., 2011), (Springmann and Cutler, 2012), (Pang et al., 2013), (Zhang and Yang, 2014), (Kok and Schön, 2016), (Särkkä et al., 2017), and (Crassidis and Cheng, 2020). Even though other techniques were proposed more recently, Foster and Elkaim's algorithm can still be used today, since it offers great accuracy and convenience for in-field applications.

In this study, we implement the calibration method proposed by Foster and Elkaim (2008) for both simulated and real sensor data. In addition, small mistakes from Foster and Elkaim (2008) are corrected, and the technique is evaluated for a limited motion scenario. The procedure performed here enhances the consumer-grade sensor HMC5883L's performance, intended primarily for integrated navigation use, by suitably compensating its systematic errors.

This paper is organized as follows. Section 2 introduces the adopted magnetometer error model; Section 3 comprehensively describes the calibration method by Foster and Elkaim (2008); in Sections 4 and 5, simulated and experimental results are displayed, respectively; Section 6, lastly, summarizes the paper and presents final thoughts and conclusions.

2. MEASUREMENT ERROR MODEL

The measurement error model adopted here, as in Foster and Elkaim (2008), includes the main systematic components that affect magnetometers: biases, scale factors, mis-

alignments, hard/soft iron errors, and random noise. Each one of them is addressed in sequence. It is important to define the scope of the calibration performed here; different classes of errors affect magnetometers, namely: constant, temperature-varying, run-to-run, and in-run contributions (Groves, 2013). The first two are often deterministic and can be compensated by the manufacturer. Run-to-run errors are those that change every time the sensor is turned on, and remain the same until it is turned off; this is the class of errors addressed here. Lastly, in-run errors appear during sensor use, and require stochastic/filtering approaches to be suitably handled.

- Biases

Often referred to as null shifts, biases are the most common error components in any sensor. They corrupt the signal by shifting it, as exemplified in Figure 1. In the context of this paper, biases move the aforementioned measurement sphere away from the origin. They are represented here as the $n \times 1$ vector $\boldsymbol{C_b}$, whose rows are the biases b_x, b_y, and b_z of each sensor, where n is the number of axes considered.

- Scale Factors

The next error components described here are the scale factors. They corrupt the measurements by scaling them at a certain factor, as displayed in Figure 2. They are represented here as the $n \times n$ diagonal matrix $\boldsymbol{C_{sf}}$, whose entries are the scale factors for each sensor, sf_x, sf_y, and sf_z.

- Misalignments

The third error component that affects magnetometers is the misalignments, or nonorthogonalities, between the three sensors' axes due to manufacturing inaccuracies. They corrupt the measurements as sensors start sensing the magnetic field from each other's axes, as shown in Figure 3, where y-axis sensor is not aligned with its
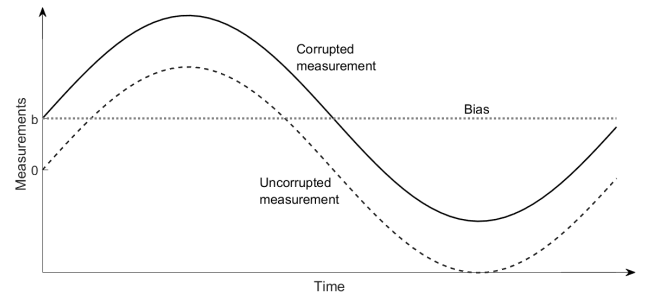

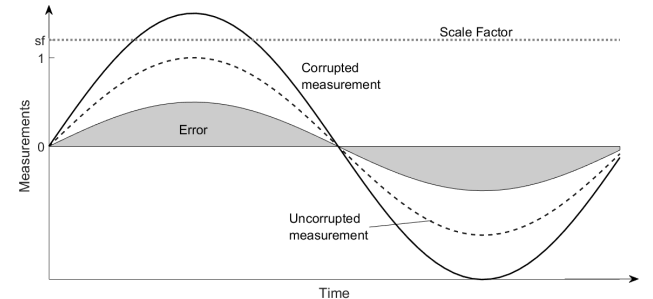Figure 1. The effect of bias on a sine wave.

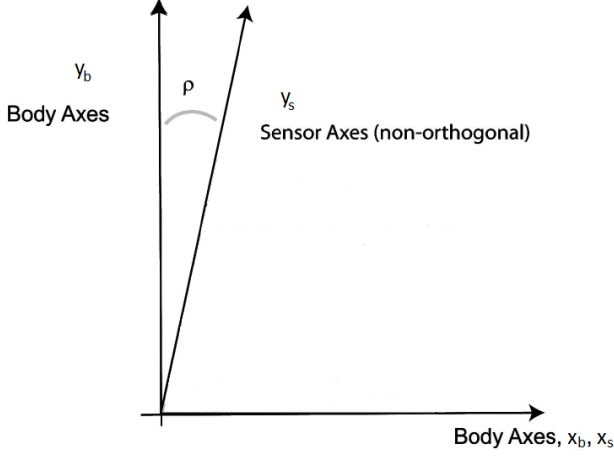Figure 2. The effect of scale factor on a sine wave.

Figure 3. An example of misalignment. (Adapted from (Foster and Elkaim, 2008))

respective body axis, causing it to sense some of x-axis' magnetic field. They are represented here by the $n \times n$ matrix $\boldsymbol{C_m}$, whose elements are trigonometric functions of the misalignment angles, namely ρ, from y-sensor to y-axis, ϕ, from z-sensor to x-z plane, and λ, from z-sensor to y-z plane.

- Random Noise

Another error that corrupts magnetometers' measurements is the random noise. In this paper, noise is considered to have a zero-mean Gaussian distribution. It is expressed as the $n \times n$ vector $\boldsymbol{C_\mu}$.

- Hard and Soft Iron

The above mentioned error components are also present in other sensors, such as accelerometers and gyroscopes. However, two other elements appear when dealing with magnetometers, namely, hard and soft iron errors, $\boldsymbol{C_{hi}}$ ($n \times 1$) and $\boldsymbol{C_{si}}$ ($n \times n$), respectively. The first is caused by undesired magnetic fields produced by materials in the sensor surroundings, such as electric circuits attached to the same casing, or the navigation equipment itself. In order to be considered a hard iron effect, the source must be attached to the same frame as the sensor, so it produces a constant contribution. On the other hand, soft iron effects are produced by ferromagnetic materials, also attached to the sensor frame, that interact with existing magnetic fields, generating another magnetic field; this relation is assumed to be linear.

Finally, accounting for each component, the measurement error model is described as follows:

$$\tilde{\boldsymbol{B}} = \boldsymbol{C_m}\boldsymbol{C_{sf}}\boldsymbol{C_{si}}(\boldsymbol{B} + \boldsymbol{C_{hi}}) + \boldsymbol{C_b} + \boldsymbol{C_\mu}, \qquad (1)$$

where $\tilde{\boldsymbol{B}}$ and $\boldsymbol{B}$ are the measured and uncorrupted magnetic field densities, respectively.

3. EXTENDED TWO-STEP CALIBRATION METHOD

The calibration method implemented here, which is an extension of Gebre-Egziabher et al. (2006), can be used both for two- or three-axial magnetometers. Since there are applications for 2D compasses, such as in maritime navigation, both cases will be presented, starting with the simplest.

3.1 Two-dimensional Calibration

The extended two-step technique is based on the idea that a pair of leveled, uncorrupted magnetometers rotated about the z-axis would produce outputs that, if plotted together, would have the shape of a centered circle with radius of B_h (total horizontal magnetic field density). Equation 2 describes this relation:

$$B_h^2 = B_x^2 + B_y^2, \qquad (2)$$

where B_x and B_y are the uncorrupted (true) magnetic field densities at x- and y-axes, respectively. However, the errors described in Section 2 reshape that circle into a shifted, rotated ellipse. Each effect can be observed in Figure 4, where δB_h stands for the combined effect of both biases and hard iron errors Foster and Elkaim (2008). Notice, however, that Gebre-Egziabher et al. (2006) attribute the shifting effect exclusively to hard iron errors.

Therefore, it is clear that the ellipse parameters are directly related to the errors. Nevertheless, notice that some error parameters are mathematically indistinguishable in that sense, since they produce the same distortions on the plotted ellipse. The shifting effect, for instance, is caused by both biases and hard iron effects. Thus, in this paper, they will be treated simply as biases ($\boldsymbol{C_b}$). Conversely, the distortions caused by soft iron effects are the same as those produced by misalignments and scale factors. Therefore, soft iron effects will be represented here as part of $\boldsymbol{C_m}$ and $\boldsymbol{C_{sf}}$. Lastly, as noise is considered to have a zero-mean, Gaussian distribution, whose effect is smoothed over the progression of the calibration method, it is not considered in the estimation model.

Based on the preceding assumptions, the measured outputs are described as follows, where the x-sensor is considered to be aligned with body axis:
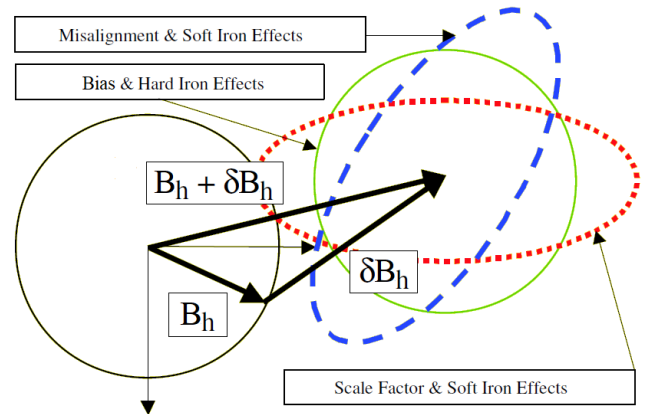
$$\tilde{B}_x = sf_x B_x + b_x \qquad (3)$$

Figure 4. Effects of error components on original circle. (Adapted from (Gebre-Egziabher et al., 2006))

$$\tilde{B}_y = sf_y(B_y cos(\rho) + B_x sin(\rho)) + b_y, \qquad (4)$$

The first step in the extended two-step calibration methodology consists of estimating the parameters that define the shifted, rotated ellipse. Without loss of generality, geometrical shapes can be represented by parametric models. In this case, the ellipse is represented as a conic section. The relation can be found, starting by solving (3) and (4) for B_x and B_y, respectively, and plugging the results into (2), yielding:

$$A\tilde{B}_x^2 + B\tilde{B}_x\tilde{B}_y + C\tilde{B}_y^2 + D\tilde{B}_x + E\tilde{B}_y + F = 0, \qquad (5)$$

Notice that (5) is linear in terms of $A, B, C, D, E,$ and F, but not in terms of the actual error parameters $b_x, b_y, sf_x, sf_y,$ and ρ. Estimates of the former parameters are found via a least squares algorithm, which requires some adjustments to (5), as follows:

$$\begin{bmatrix} \tilde{B}_x^2 & \tilde{B}_x\tilde{B}_y & \tilde{B}_x & \tilde{B}_y & 1 \end{bmatrix} \begin{bmatrix} \dfrac{A}{C} \\[4pt] \dfrac{B}{C} \\[4pt] \dfrac{D}{C} \\[4pt] \dfrac{E}{C} \\[4pt] \dfrac{F}{C} \end{bmatrix} = -\tilde{B}_y^2 \qquad (6)$$

Next, all measurements are combined into matrix $\mathbf{H}$, as follows:

$$\mathbf{H} \times \mathbf{X} = \mathbf{Y}, \qquad (7)$$

with

$$\mathbf{X} = \begin{bmatrix} \dfrac{A}{C} & \dfrac{B}{C} & \dfrac{D}{C} & \dfrac{E}{C} & \dfrac{F}{C} \end{bmatrix}^T, \qquad (8)$$

$$\mathbf{Y} = \begin{bmatrix} -\tilde{B}_{y1}^2 & -\tilde{B}_{y2}^2 & . & . & . & -\tilde{B}_{yk}^2 \end{bmatrix}^T, \qquad (9)$$

$$\mathbf{H} = \begin{bmatrix} \tilde{B}_{x1}^2 & \tilde{B}_{x1}\tilde{B}_{y1} & \tilde{B}_{x1} & \tilde{B}_{y1} & 1 \\ \tilde{B}_{x2}^2 & \tilde{B}_{x2}\tilde{B}_{y2} & \tilde{B}_{x2} & \tilde{B}_{y2} & 1 \\ . & . & . & . & . \\ . & . & . & . & . \\ \tilde{B}_{xk}^2 & \tilde{B}_{xk}\tilde{B}_{yk} & \tilde{B}_{xk} & \tilde{B}_{yk} & 1 \end{bmatrix} \qquad (10)$$

where k is the epoch of each measurement taken.

Lastly, (11) is the least squares solution:

$$\hat{\mathbf{X}} = (\mathbf{H}^T\mathbf{H})^{-1}\mathbf{H}^T\mathbf{Y} \qquad (11)$$

where $\hat{\mathbf{X}}$ are the estimated parameters that best fit the ellipse. Notice that, in (Foster and Elkaim, 2008), there is an error in the least squares equation, and the matrices $\mathbf{H}$, $\mathbf{X}$, and $\mathbf{Y}$ are defined slightly differently. Finally, $b_x, b_y,$ $sf_x, sf_y,$ and ρ, are functions of $A, B, C, D, E,$ and F, and can be calculated either algebraically or numerically, as

long as B_h is known. The latter is easily computed through world magnet field models, as the US/UK World Magnetic Model (WMM) and International Geomagnetic Reference Field (IGRF) (Chulliat et al., 2015; Thébault et al., 2015).

3.2 Three-dimensional Calibration

The three-dimensional calibration follows the ideas described in Section 3.1. However, instead of calculating the parameters of an ellipse, defined as a conic section, the objective now is to estimate the parameters of a shifted, rotated ellipsoid, defined as a quadric surface. Firstly, the parametrization of the z-axis' measurements is necessary:

$$\begin{aligned} \tilde{B}_z = sf_z[B_z cos(\phi)cos(\lambda) + B_x sin(\phi)cos(\lambda) \\ + B_y sin(\lambda)] + b_z \end{aligned} \qquad (12)$$

In addition, instead of taking the horizontal magnetic field magnitude B_h as a reference, the total magnetic field intensity B_t is necessary. The relation described in (13) suggests, analogously to (2), that the magnitude of the vectors B_x, B_y, and B_z always falls onto the surface of a sphere with radius B_t:

$$B_t^2 = B_x^2 + B_y^2 + B_z^2 \qquad (13)$$

The ellipsoid whose parameters are to be estimated is described by the quadric surface general equation (14). Notice again, that there is a small typing error in this equation at the original work by Foster and Elkaim (2008).

$$\begin{aligned} A\tilde{B}_x^2 + B\tilde{B}_x\tilde{B}_y + C\tilde{B}_x\tilde{B}_z + D\tilde{B}_y^2 + E\tilde{B}_y\tilde{B}_z \\ + F\tilde{B}_z^2 + G\tilde{B}_x + H\tilde{B}_y + I\tilde{B}_z + J = 0, \end{aligned} \qquad (14)$$

Again, the ellipsoid parameters are functions of the sought error parameters, and the relation between them can be found algebraically (or numerically). Finally, the same solution for the 2D case is employed here, adapting $\mathbf{H}$, $\mathbf{X}$, and $\mathbf{Y}$, and using them for solving the least squares problem of (11).

4. SIMULATED EXPERIMENTS

Before actual hardware implementation, simulations were performed in order to confirm that the algorithm was properly running, and to analyze its performance in the expected scenario. Corrupted data were generated based on the model from (1); the error parameters were set in accordance with Honeywell HMC5883L datasheet, the triaxial magnetometer used in Section 5.

4.1 Two-dimensional Calibration

In the first tested scenario, a 2D calibration was performed. As mentioned before, this version of the technique is useful when only two axes are available (or required). In this case, sensors must be horizontally leveled and are rotated about the z-axis. Accordingly, 3600 samples of corrupted magnetometer measurements were generated at frequency of 15Hz, while rotating in yaw with constant rate of $10°/s$; the error parameters corrupting the signal are given

in Table 1. Noise was defined as a zero-mean Gaussian distribution with variance of $2mG^2$ throughout this entire section. Figure 5 shows the corrupted and corrected data, and a reference circle with radius B_h. Notice that the corrupted data assume the shape of a shifted, rotated ellipse, while the calibrated data lies on top of the expected circle.

The correction displayed in Figure 5 was preceded by the error parameters estimation, whose results are given in Table 1. As can be inferred, satisfactory accuracy was obtained with Foster and Elkaim's method for two-dimensional case.

4.2 Three-dimensional Calibration

For the three-dimensional simulation, 60000 samples were generated at the same conditions of Section 4.1, except for the error parameters, which are summarized in Table 2. In addition, instead of one, 17 rotations in yaw, with different initial roll and pitch angles were carried out (Figure 6).

The three-dimensional algorithm by Foster and Elkaim (2008) was used, and the estimated error parameters (jointly with their MSEs) are given in Table 2. After compensating for the estimated errors, the corrected measurements lie on top of the reference sphere, confirming the procedure's effectiveness (Figure 7).

In conclusion, the algorithm worked appropriately for both cases, which enabled us to proceed to hardware implementation.

Table 1. Two-dimensional calibration results for simulated data

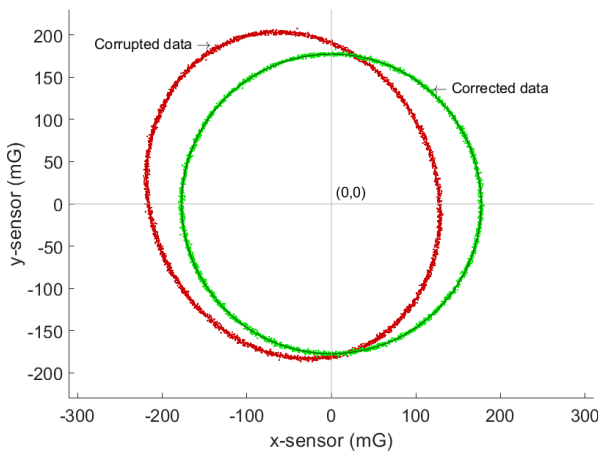| Error component	Original	Estimated	MSE	Unit
b_x	45	-44.9938	3.8703×10^{-5}	mG
b_y	10	9.9994	3.5101×10^{-7}	mG
sf_x	0.98	0.9801	8.7677×10^{-9}	unitless
sf_y	1.09	1.0898	4.2450×10^{-8}	unitless
ρ	-6	-6.0305	2.8316×10^{-7}	°

Figure 5. This figure shows corrupted and corrected data, in red and green, respectively. In addition, the expected uncorrupted circle is plotted in dark green.

Table 2. Three-dimensional calibration results for simulated data

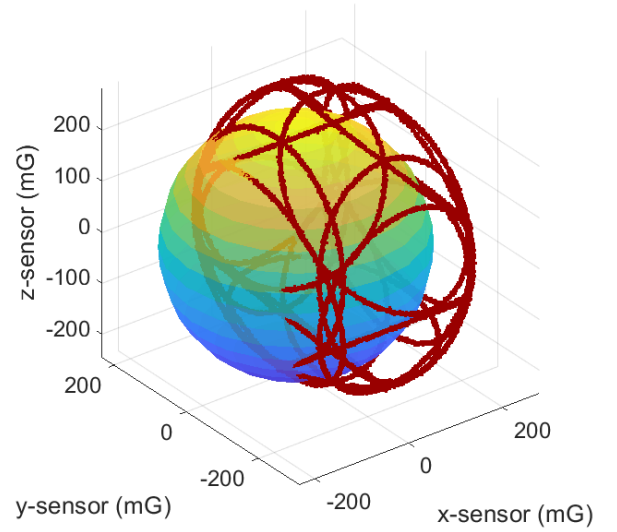| Error component	Original	Estimated	MSE	Unit
b_x	50	50.0045	2.0370×10^{-5}	mG
b_y	-40	-39.9946	2.8869×10^{-5}	mG
b_z	20	19.9932	4.6853×10^{-5}	mG
sf_x	0.96	0.9604	1.6561×10^{-7}	unitless
sf_y	1.15	1.1496	1.3744×10^{-7}	unitless
sf_z	1.11	1.1102	3.0309×10^{-8}	unitless
ρ	3	3.0032	1.0181×10^{-5}	°
ϕ	-2	-1.9927	5.3474×10^{-5}	°
λ	6	6.0067	4.4481×10^{-5}	°

Figure 6. Generated corrupted measurements, in red, plotted with the reference sphere of radius B_t.
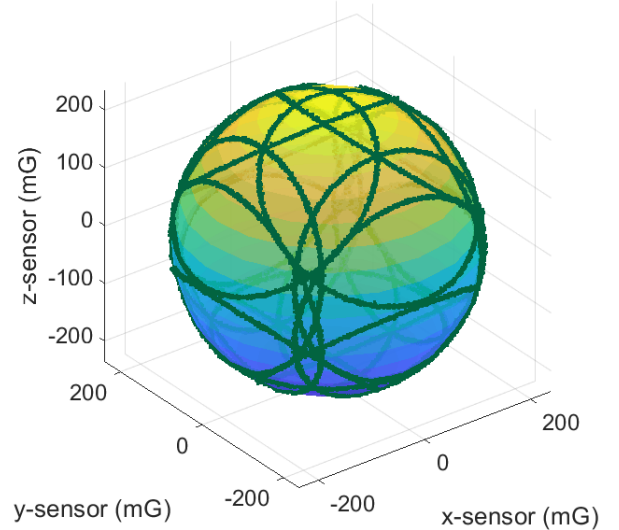

Figure 7. Corrected measurements, in green, plotted with the reference sphere of radius B_t.

5. HARDWARE IMPLEMENTATION

In this section, the Integrated Circuit (IC) HCM5883L by Honeywell, containing a consumer-grade, triaxial mag-

netometer was used to validate the extended two-step calibration technique. The measurements were sampled at a frequency of 15Hz, which is the default option. The IC built-in Analog-to-Digital Converter (ADC) offers a 12-bit digital resolution. Conversely, there is a trade-off between magnetic field resolution and measurement range. The default option (which was used) is 0.92mG/LSb and ±1300mG, respectively.

Since the extended two-step technique is intended to enable in-field calibration of magnetometers, with no equipment or external source of heading, the rotation movements were performed by hand. Two data sets were collected, with the first one containing 17200 samples. Figure 8 displays the measurements and reference sphere.

After parameter estimation and algebraic computation, the error parameters were obtained, as summarized in Table 3. Figure 9 shows the corrected measurements, successfully lying on top of the reference sphere, whose radius was calculated via the WMM. Figure 10(a) displays the difference between measured and expected magnitude, before and after calibration.

Notice that, although the calibrated measurements stand very close to the sphere of Figure 9 and have magnitude near expected (Figure 10(a)), they do not present the same uniformity as in the simulated cases. This is a result of
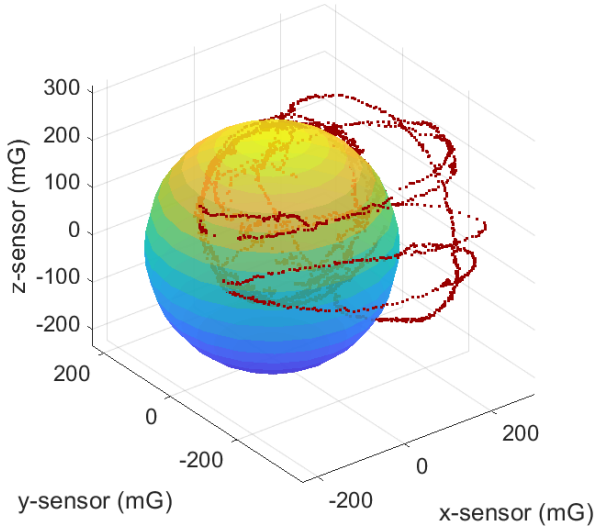

Figure 8. Corrupted measurements of the first scenario, in red, plotted with the reference sphere of radius B_t, computed via the WMM.

Table 3. Three-dimensional calibration results for real data, first scenario.

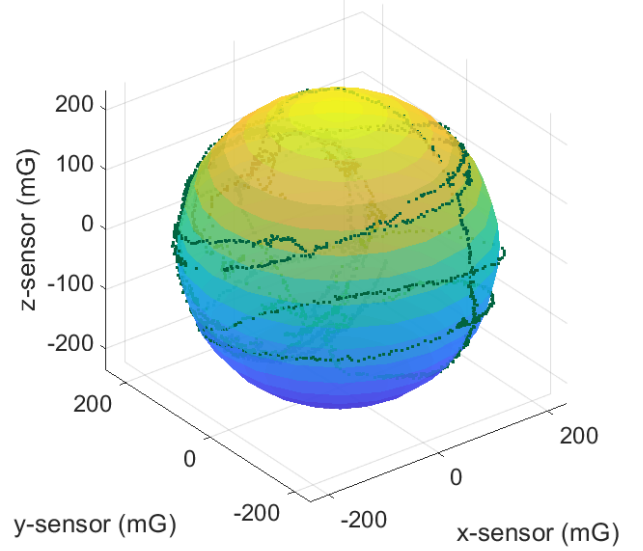| Error component	Estimated	Unit
b_x	46.6374	mG
b_y	-144.7348	mG
b_z	106.5259	mG
sf_x	1.1401	unitless
sf_y	1.0662	unitless
sf_z	1.1102	unitless
ρ	0.9467	°
ϕ	-3.4458	°
λ	0.3638	°

Figure 9. Corrected measurements of the first scenario, in green, plotted with the reference sphere of radius B_t, computed via the WMM.
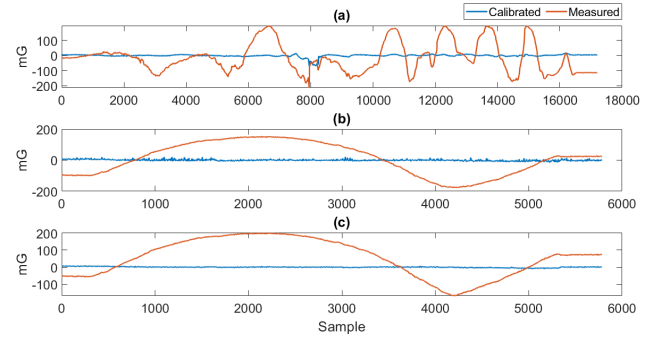

Figure 10. Difference between the magnitude of corrupted and corrected measurements, and expected magnitude. (a) three-dimensional estimation, unrestricted motion scenario. (b) three-dimensional estimation, restricted motion scenario. (c) two-dimensional estimation, restricted motion scenario.

other errors, not considered in this model, including non-deterministic and time-varying components, that affect the magnetometers readings. However, such circumstances require different estimation approaches, which are not the focus of this work. Still, the method performed appropriately for what it was intended, even with less samples than in the simulated case.

The second data set was meant to represent a restricted scenario where only limited motion is possible, such as in a land, or maritime vehicle application. In this case, the vehicle was supposed not being able to perform the same rotations as in Figure 9. Even though this is beyond the scope defined by the authors, we tested the three-dimensional, extended two-step methodology for a scenario where yaw is almost the only movement possible. Figure 11 shows the sampled data and the reference ellipsoid.

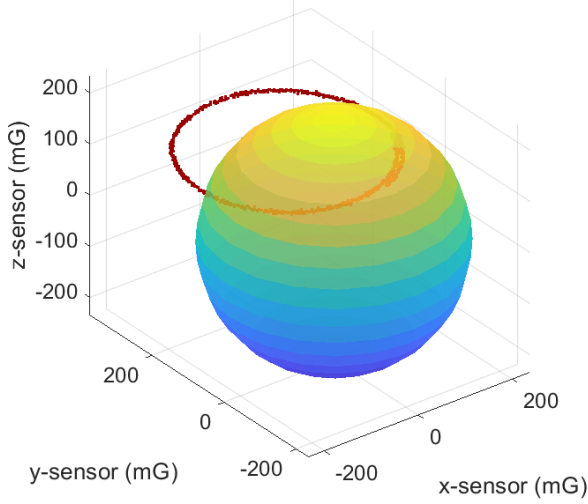However, after calibration, measurements were not all adequately corrected. Au contraire, the erroneous estimation

Figure 11. Corrupted, restricted measurements, in red, plotted with the reference sphere of radius B_t, computed via the WMM.

Table 4. Calibration results for real data, second scenario

Error component	3D Calibration	2D Calibration	Unit
b_x	42.1704	41.0439	mG
b_y	185.0259	185.2486	mG
b_z	75.1705	-	mG
sf_x	0.8391	1.1050	unitless
sf_y	0.7917	1.0486	unitless
sf_z	0.0876	-	unitless
ρ	-2.4289	-2.4280	°
ϕ	6.2294	-	°
λ	44.5829	-	°

of the error parameters, especially for λ (Table 4), caused some measurements to become even more incorrect, as displayed in Figure 12. Therefore, despite producing a consistent result in terms of the leastsquares estimation, the three-dimensional method seems to be appropriate only for cases where rotation is not so restricted (Figure 10(b)). Although the algorithm was capable of finding a reasonable fit with respect to B_t, the lack of data mislead the parameter estimation, producing unreasonable estimates as $\hat{\lambda} = 44.5829°$.

Lastly, we assumed a two-dimensional magnetometer in the restricted scenario, not considering measurements from z-sensor, and we conducted calibration using the two-dimensional algorithm of Section 3.1. Again, this test is beyond the scope defined by Foster and Elkaim (2008), since the data of the restricted scenario were sampled while the sensor was being rotated by hand, and there is no guarantee it was horizontally leveled at any point. Figure 13 shows the 2D corrupted and corrected data plotted with the reference circle, Figure 10(c) displays the least squares performance with respect to B_t, and Table 4 contains the estimated parameters, which were close to the ones obtained with the 3D technique (second scenario). Therefore, for estimating the error parameters of x- and y-sensors in the restricted scenario, the two-dimensional algorithm seems to be appropriated, even without a precise leveling.
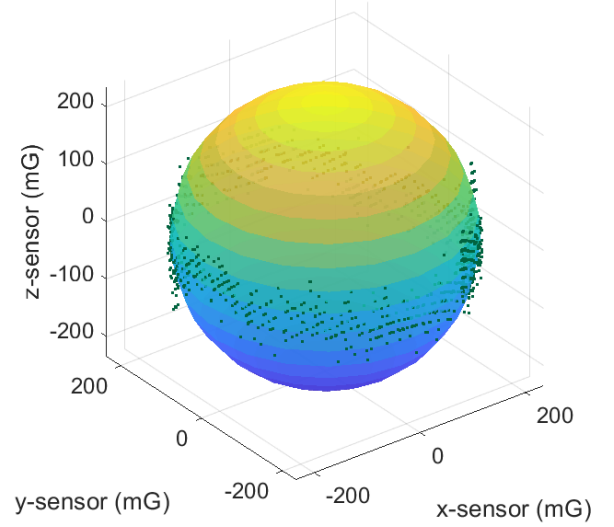

Figure 12. Corrected, restricted measurements, in green, plotted with the reference sphere of radius B_t.
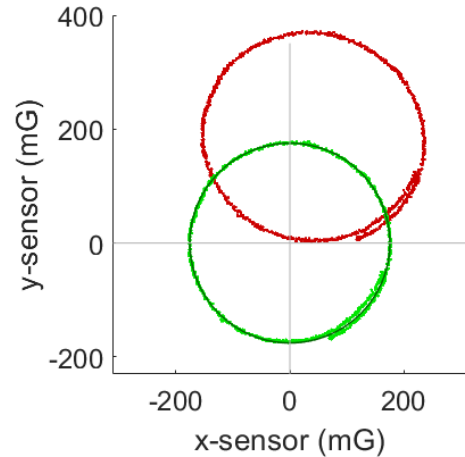

Figure 13. Corrupted and corrected measurements, in red and green, respectively, for x- and y-sensors, plotted with the reference circle of radius B_h.

6. CONCLUSIONS

In this paper, we revised the subject of magnetometer calibration, which was defined as the scope of study. Error models, suitable for calibration were defined and the calibration procedures by Foster and Elkaim (2008) were thor-

oughly described, pointing a few mistakes in the original paper. Results from simulated and hardware implementation of the calibration technique were proposed, evidencing successful estimation of the expected error parameters and subsequent correction of measurements, with degraded performance for the restricted motion scenario introduced here. In conclusion, the methodology by Foster and Elkaim (2008) properly performed the calibration of the consumer-grade HMC5883L triaxial magnetometer, enhancing its reliability, and making it more appropriate for applications like integrated navigation.

For future studies, we consider relevant the implementation of the extended two-step technique for accelerometer calibration, since Foster and Elkaim (2008) claimed it is also applicable, although not tested (Menezes Filho et al., 2020). In addition, finding analytical closed-form solution mapping the ellipse/ellipsoid parameters to the actual error parameters would facilitate implementation and reduce computational effort. [1]

REFERENCES

Alonso, R. and Shuster, M.D. (2002b). Complete linear attitude-independent magnetometer calibration. *Journal of the Astronautical Sciences*, 50(4), 477–490.

Alonso, R. and Shuster, M.D. (2002a). TWOSTEP: A fast robust algorithm for attitude-independent magnetometer-bias determination. *Journal of the Astronautical Sciences*, 50(4), 433–452.

Bowditch, N. (1995). *The american practical navigator*. Defense Mapping Agency Hydrographic/Topographic Center, Greenbelt, Md.

Chulliat, A., Macmillan, S., Alken, P., Beggan, C., Nair, M., Hamilton, B., Woods, A., Ridley, V., Maus, S., and Thomson, A. (2015). The US/UK world magnetic model for 2015-2020.

Crassidis, J.L. and Cheng, Y. (2020). Three-axis magnetometer calibration using total least squares. In *AIAA Scitech 2020 Forum*, 1688.

Crassidis, J.L., Lai, K.L., and Harman, R.R. (2005). Real-time attitude-independent three-axis magnetometer calibration. *Journal of Guidance, Control, and Dynamics*, 28(1), 115–120.

Foster, C.C. and Elkaim, G.H. (2008). Extension of a two-step calibration methodology to include nonorthogonal sensor axes. *IEEE Transactions on Aerospace and Electronic Systems*, 44(3), 1070–1078.

Gambhir, B. (1975). Determination of magnetometer biases using module RESIDG. *Computer Sciences Corporation, Report*, (3000-32700), 01.

Gebre-Egziabher, D., Elkaim, G.H., David Powell, J., and Parkinson, B.W. (2006). Calibration of strapdown magnetometers in magnetic field domain. *Journal of Aerospace Engineering*, 19(2), 87–102.

Gebre-Egziabher, D., Hayward, R.C., and Powell, J.D. (1996). A low-cost GPS/inertial attitude heading reference system (AHRS) for general aviation applications. In *IEEE 1998 Position Location and Navigation Symposium (Cat. No. 98CH36153)*, 518–525. IEEE.

Groves, P.D. (2013). *Principles of GNSS, inertial, and multisensor integrated navigation systems*. Artech house.

Kok, M. and Schön, T.B. (2016). Magnetometer calibration using inertial sensors. *IEEE Sensors Journal*, 16(14), 5679–5689.

Menezes Filho, R.P., Silva, F.O., and Vieira, L.A. (2020). Triaxial accelerometer calibration using an extended two-step methodology. In *IEEE Latin American Robotics Symposium (under review)*.

Pang, H., Zhang, Q., Wang, W., Wang, J., Li, J., Luo, S., Wan, C., Chen, D., Pan, M., and Luo, F. (2013). Calibration of three-axis magnetometers with differential evolution algorithm. *Journal of Magnetism and Magnetic Materials*, 346, 5–10.

Renaudin, V., Afzal, M.H., and Lachapelle, G. (2010). New method for magnetometers based orientation estimation. In *IEEE/ION Position, Location and Navigation Symposium*, 348–356. IEEE.

Särkkä, O., Nieminen, T., Suuriniemi, S., and Kettunen, L. (2017). A multi-position calibration method for consumer-grade accelerometers, gyroscopes, and magnetometers to field conditions. *IEEE Sensors Journal*, 17(11), 3470–3481.

Sheng, H. and Zhang, T. (2015). MEMS-based low-cost strap-down AHRS research. *Measurement*, 59, 63–72.

Springmann, J.C. and Cutler, J.W. (2012). Attitude-independent magnetometer calibration with time-varying bias. *Journal of Guidance, Control, and Dynamics*, 35(4), 1080–1088.

Thébault, E., Finlay, C.C., Beggan, C.D., Alken, P., Aubert, J., Barrois, O., Bertrand, F., Bondar, T., Boness, A., Brocco, L., et al. (2015). International geomagnetic reference field: the 12th generation. *Earth, Planets and Space*, 67(1), 79.

Vasconcelos, J.F., Elkaim, G., Silvestre, C., Oliveira, P., and Cardeira, B. (2011). Geometric approach to strapdown magnetometer calibration in sensor frame. *IEEE Transactions on Aerospace and Electronic systems*, 47(2), 1293–1306.

Zhang, Z.Q. and Yang, G.Z. (2014). Micromagnetometer calibration for accurate orientation estimation. *IEEE Transactions on Biomedical Engineering*, 62(2), 553–560.

---

[1] In order to encourage and help the interested readers to implement this calibration technique, the algorithms and data used in this study are available at the authors' Research Gate profiles.